Journal of
Instrumentation

Microwave diagnostic at Wendelstein 7-X

Published by IOP Publishing for Sissa Medialab

Received: *August 28, 2025*
Revised: *October 22, 2025*
Accepted: *November 2, 2025*
Published: *December 5, 2025*

21st International Symposium on Laser-Aided Plasma Diagnostics
Saillon, Switzerland
1–5 September 2025

Microwave diagnostic at Wendelstein 7-X

A. Krämer-Flecken[a,*] **N. Chaudhary**[b] **J. Guerrero Arnaiz**[b] **M. Hirsch**[b] **D. López-Rodríguez**[c] **D. Moseev**[b] **H. Oosterbeek**[b] **G. Weir**[b] **T. Windisch**[b] **D. Carralero**[d] **T. Estrada**[d] **X. Han**[e] **E. Maragkoudakis**[b] **V. Murugesan**[b] **V. Nair**[b] **S. Ponomorenko**[b] **and the W7-X Team**

[a] *Forschungszentrum Jülich GmbH, Institute of Fusion Energy and Nuclear Waste Management – Plasma Physics, 52425 Jülich, Germany*
[b] *Max Planck Institut für Plasmaphysik, 17491 Greifswald, Germany*
[c] *Laboratory for Plasma Physics, LPP-ERM/KMS, Brussels, Belgium*
[d] *Laboratorio Nacional de Fusión-CIEMAT, Madrid, Spain*
[e] *University of Wisconsin-Madison, Madison, WI 53706, U.S.A.*

E-mail: a.kraemer-flecken@fz-juelich.de

Abstract: At Wendelstein 7-X (W7-X), the world's largest superconducting stellarator with a five-fold symmetry and reduced neoclassical transport, a broad suite of microwave diagnostics is installed and operated. Due to the robustness of in-vessel components and transmission lines against the harsh environment in fusion devices, they are candidates for reactor plasma control.
This presentation will show an overview of microwave diagnostics at W7-X. After introducing the governing equations for the propagation of microwaves in a fusion plasma e.g. the determination of the local positions where the measurements are performed, the different diagnostics are presented. The presentation will encompass the installed diagnostics, but also, the planned upgrades and show important technical details and highlighting results obtained during the last campaigns. It will cover passive microwave diagnostics for the estimation of the electron temperature profile by radiometry from the 2nd and 3rd harmonic of the electron cyclotron emission (ECE) with a temporal resolution in the

See Klinger et al. 2019 (https://doi.org/10.1088/1741-4326/ad2f4d) for the W7-X Team.

*Corresponding author.

https://doi.org/10.1088/1748-0221/20/12/C12008

MHz-range. Furthermore, the 1st–3rd harmonic ECE radiation is measured with interferometry for both, X- and O-mode polarization. Also, fluctuations of the electron temperature are measured by various methods of correlation ECE. Active probing radar applications, so-called reflectometry, are installed to measure density fluctuations and its propagation. They allow measuring the turbulence propagation for a wide wavenumber range. Under certain assumptions the radial electric field, an important quantity for the neoclassical transport is deduced from this propagation. To measure the electron density profile in the edge, a frequency modulated continuous wave reflectometer is installed in the Ion Cyclotron Resonance Heating (ICRH)-antenna. The purpose of the instrument is the measurement of the density profile to improve the coupling of the ICRH-waves into the plasma. Besides this, the measurement of the density profile in the edge with high spatial and temporal resolution is independent of the ICRH-operation. Furthermore, a microwave scattering diagnostic, the collective Thomson Scattering (CTS), uses a gyrotron as active probing beam yields direct information of the ion temperature of hydrogen or in later campaigns deuterium species and does not rely on the impurity temperature.

KEYWORDS: Interferometry; Microwave radiometers; Nuclear instruments and methods for hot plasma diagnostics; Plasma diagnostics - interferometry, spectroscopy and imaging

2025 JINST 20 C12008

Contents

1 Introduction

Microwave radiation refers to a type of electromagnetic radiation with frequencies ranging from approximately 0.3 GHz to 300 GHz. They occupy the portion of the electromagnetic spectrum between radio waves and infrared radiation. Microwave based diagnostic in high temperature plasmas [1, 2] are quite successful for two reasons: (i) they allow the measurement of important plasma quantities e.g. electron temperature and electron density profiles across a major plasma part of the plasma radius as well as fluctuations in both quantities due to the high spatial and temporal resolution and (ii) as they have fewer demands on the optical path and optical components e.g. mirrors it makes them an ideal diagnostic in the harsh environment of recent experiments as well as in future fusion reactors. Microwave radiation, when not transmitted via quasi optical beam lines, can easily be guided in wave guides, either oversized or fundamental ones, and they can be bent around corners widening the application range.

There are two main applications in plasma physics, (i) passive measurement of microwave radiation from the plasma and (ii) the active probing of microwave radiation using properties of the plasma at reflection layers.

The range of microwave frequencies, applied in high temperature plasma diagnostic, depends mainly on the parameters of the fusion device, for which they are designed and developed. An important quantity is the magnetic field of the device, as it defines the gyration frequency. This frequency plays an important role in the determination of resonances and cut-off layers, as outlined in section 2. Also, the plasma density plays an important role for the determination of the cut-off and resonance layers. The design of a microwave diagnostic has to be adjusted to these parameters. In this paper, the microwave diagnostic for the stellarator Wendelstein 7-X (W7-X) are presented. W7-X [3, 4] is the world's largest stellarator of HELIAS-type with a mean major radius of $R = 5.5\,\mathrm{m}$,

2025 JINST 20 C12008

and minor radius of $a = 0.52\,\mathrm{m}$. The plasma volume is $V \approx 30\,\mathrm{m}^3$, depending on the magnetic configuration [5]. The device allows the operation in different magnetic configurations, characterized by the edge iota (ι). W7-X has a five-fold symmetry, and the spatial structure of the magnetic field is designed to keep the neoclassical transport at a minimum. Each of the five segments consist of 10 non-planar and 4 planar coils, generating a magnetic structure with an island chain outside the last closed flux surface (LCFS) in the standard configuration having $\iota = 1$. In addition, control coils are included for the modulation of the island size and position. The toroidal magnetic field of W7-X amounts to $B_t = 2.5\,\mathrm{T}$ on-axis, during the majority of programs in the last experiment campaigns. However, the device is also operated at a lower magnetic field of $B_t = 1.8\,\mathrm{T}$ to achieve an enhanced plasma beta. Due to the water cooled in vessel components, W7-X is capable to conduct plasma pulses up to a duration of 30 min. Since W7-X is a stellarator it has no toroidal symmetry and the plasma cross-section changes from a bean shaped cross-section to a triangular cross-section and back. This makes the installation of those microwave diagnostics difficult, which need an increasing magnetic field strength along their line of sight for the measurement. This condition is achieved for cross-sections which are sufficiently close to the bean shaped plasma cross-section. W7-X is mainly heated by electron cyclotron resonance heating (ECRH) [6] at a frequency of $f = 140\,\mathrm{GHz}$. Beside a nominal available ECRH power of 10 MW, neutral beam heating of $P_{\mathrm{NBI}} = 7\,\mathrm{MW}$ for a duration $\leq 10\,\mathrm{s}$ is available. W7-X employs a range of advanced microwave diagnostics to investigate the plasma, including density, temperature, and turbulence properties. These diagnostics utilize microwave radiation to probe the plasma in a non-invasive and high-resolution way. They play a crucial role in understanding plasma stability, transport, and confinement, supporting the optimization of W7-X's performance and advancing the development of stellarator-based fusion energy.

The rest of the paper discusses the installed and planned microwave diagnostics for W7-X. After giving a short overview on the governing equations for microwaves propagation in a plasma in section 2, the passive microwave diagnostics, such as Michelson interferometer and heterodyne radiometry both measuring the emitted Electron-Cyclotron-Emission (ECE) from the plasma, are discussed. Also, different flavours of radiometry diagnostics, such as correlation and imaging systems are discussed in section 3. In section 4 microwave diagnostic probing plasma quantities at the cut-off positions e.g. density and rotation are presented. It includes also a section on the CTS diagnostic delivering the ion temperature of bulk ions is in the plasma core. The paper concludes with section 5.

2 Basic equations for microwave propagation in plasmas

In plasma physics, the Appleton equation [7, 8] is used to analyse phenomena such as wave-particle interactions, wave propagation, and refraction in magnetized plasmas. It relates the refractive index N with the probing frequency ω and the fundamental plasma- and electron cyclotron frequency.

$$N^2 = 1 - \frac{A \cdot (1 - A)}{1 - A - 1/2B^2 \sin^2\theta \pm C} \tag{2.1}$$

$$A = \frac{\omega_{pe}^2}{\omega^2}; \quad B = \frac{\omega_{ce}}{\omega}$$

$$C = \left[\left(1/2B^2 \sin^2\theta\right)^2 + (1 - A)^2 B^2 \cos^2\theta\right]^{1/2}$$

2025 JINST 20 C12008

Here ω_{pe} denotes the plasma frequency and ω_{ce} the cyclotron frequency:

$$\omega_{pe} = \sqrt{\frac{n_e e^2}{\epsilon_0 m_e}}; \quad \omega_{ce} = \frac{eB}{m_e \gamma} \tag{2.2}$$

γ takes into account relativistic effects, e denotes the electron charge, m_e the electron mass, n_e is the local electron density and B the local magnetic field. The angle θ in eq. (2.1) denotes the angle between the wave vector and the magnetic field. In the case, $\theta = 0$ the propagation is parallel to the magnetic field and for $\theta = \pi/2$ perpendicular. In this case, two solutions for the refractive index are possible, depending on whether the electric field vector of the wave $\mathbf{E}$ is parallel to the magnetic field (*O-Mode*) or perpendicular (*X-Mode*). The refractive index for the latter case is given in eq. (2.3).

$$\begin{aligned} &\text{O-Mode} \qquad N_O^2 = 1 - \frac{\omega_{pe}^2}{\omega^2} \\ &\text{X-Mode} \qquad N_X^2 = 1 - \frac{\omega_{pe}^2 \left(\omega^2 - \omega_{pe}^2\right)}{\omega^2 \left(\omega^2 - \omega_{pe}^2 - \omega_{ce}^2\right)} \end{aligned} \tag{2.3}$$

In case of a vanishing refractive index ($N = 0$) a cut-off condition is reached, and the wave is reflected. Frequencies fulfilling the cut-off condition can be deduced from eq. (2.3), for O- and X-mode propagation separately, by solving eq. (2.3) for ω.

$$\begin{aligned} &\text{O-Mode} \qquad \omega_{\mathrm{CO}} = \omega_{pe} \\ &\text{X-Mode} \qquad \omega_{\mathrm{CO1,2}} = \left(\frac{2\omega_{pe}^2 + \omega_{ce}^2}{2} \pm \sqrt{\frac{\left(2\omega_{pe}^2 + \omega_{ce}^2\right)^2}{4} - \omega_{pe}^4} \right)^{1/2} \end{aligned} \tag{2.4}$$

The frequencies for cut-off conditions depend on the local magnetic field and on the local density of the plasma. All active microwave diagnostics make use of eq. (2.4) to measure local plasma quantities at the cut-off position, regardless of being applied in fusion plasmas, mobile communication, material inspection or climate research. In the case $N = \infty$ a resonance condition is achieved, and the power carried by a wave at this frequency is absorbed as it is the case e.g. for ECRH-heating.

Having a spatially varying toroidal magnetic field which increases with the distance to the observer, a relation between the emitted frequency of the plasma and the location within the plasma is possible. This condition allows measuring electron temperature profiles in the plasma. In the case of a Maxwellian energy distribution of the electrons, the intensity of the emitted radiation can be related to the temperature. The ECE-spectrum can be described by Planck's equation. In a fusion plasma $\hbar\omega \ll kT_e$ is fulfilled and the Rayleigh-Jeans approximation can be used for optically thick emission.

$$I(\omega) = \frac{\omega^2 \cdot T_e}{8 \cdot \pi^3 \cdot c^2} \tag{2.5}$$

where $I(\omega)$ is the specific intensity. The measurement of the intensity of the emitted frequency alone is not sufficient. Also, the transport of the radiation from its point of emission across the plasma to the observing antenna has to be taken into account, including reflections from the wall. The transport of the radiation is described by

$$\frac{dI}{ds} = j(\omega) - I \cdot \alpha(\omega) \tag{2.6}$$

2025 JINST 20 C12008

where s is the ray path and α the absorption coefficient and j the emissivity, which are itself a function of the frequency. The transport can be described by the optical depth (τ) defined by:

$$\tau(\omega) = 2 \int \alpha(\omega) ds \tag{2.7}$$

which adds a correction term $(1 - e^{-\tau})$. The absorption coefficient is itself a function of local plasma parameters as n_e, T_e, the polarization of the wave and the harmonic number [7]. In addition, reflection from the wall plays a role in case of small τ and the radiation temperature (T_e^{rad}) has to be corrected by the reflectivity ρ, yielding:

$$T_e^{\mathrm{rad}} = \frac{\omega^2 \cdot T_e}{8 \cdot \pi^3 \cdot c^2} \cdot \frac{(1 - e^{-\tau})}{(1 - \rho e^{-\tau})} \tag{2.8}$$

To overcome the problem with reflections from the wall often tiles with a roof-top like structure are positioned on the surface illuminated by the antenna pattern [9]. With respects to cut-off's a suitable measurement of the electron temperature is performed for X-mode perpendicular propagation $\theta = 90°$. For optical thick plasmas ($\tau \gg 1$) the correction term in eq. (2.8) becomes small and eq. (2.5) can be applied.

3 Passive microwave diagnostics

This section discusses the passive microwave application at W7-X. They consist of the Michelson Interferometer to measure the ECE spectrum up to the 4$^{\mathrm{th}}$ harmonics and a heterodyne radiometer diagnostic. The latter determines the electron temperature (T_e)-profile across a major part of the plasma radius and makes use of the 2$^{\mathrm{nd}}$- and sometimes the 3$^{\mathrm{rd}}$-harmonic in case the local density increases the upper cut-off frequency for the 2$^{\mathrm{nd}}$-harmonic. A W-band radiometer is installed for operation at $B_t = 1.8\,\mathrm{T}$. Furthermore, the correlation ECE will be presented, which is installed for the measurement of T_e-fluctuations. All diagnostics make use of the same sight line defined by a Gaussian optics. Beside the presently active diagnostics, this section will end with thoughts on a planned ECE-imaging diagnostic for W7-X.

3.1 Michelson interferometer

A Michelson interferometer of Martin-Puplett type is installed close to the bean-shaped plasma cross-section at W7-X [10–12]. It shares the optical front end together with the heterodyne radiometers. The front end of the instrument [17] is shown in figure 1 and consists of a Gaussian telescope consisting of 4 mirrors, focussing the radiation from the plasma into a horn antenna. The Gaussian beam waist for $f = 140\,\mathrm{GHz}$ is $w_0 \leq 23\,\mathrm{mm}$ and varies only by 2 mm across the plasma diameter, to achieve equal radiating volume size across the plasma diameter. The horn antenna is an extremely broad band conical horn antenna [13], with a beam waist $\propto \sqrt{1/f}$. After a power splitter and a polarisation tuner, the radiation passes the bio shield and a notch filter to exclude the 140 GHz stray radiation from the gyrotrons sustaining the discharge. The total transmission line amounts to $\approx 24\,\mathrm{m}$ with a total loss of 21 dB. The interferometer covers the frequency range of 50 GHz to 500 GHz where the 1$^{\mathrm{st}}$ to 4$^{\mathrm{th}}$ harmonic at W7-X is expected. Due to the high aspect ratio, each single harmonic is well resolved and with no overlap between harmonics. To measure the interferogram the mirror

2025 JINST 20 C12008

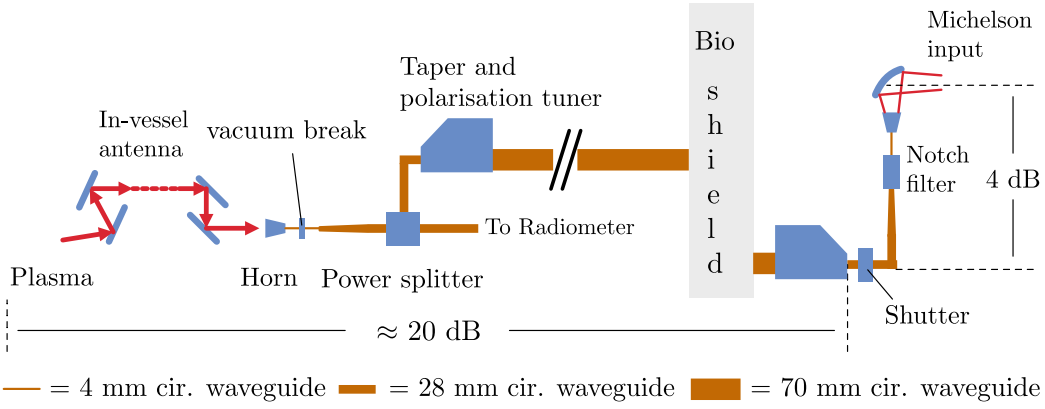

Figure 1. The schematic view of the front end of the Michelson interferometer at W7-X. Reproduced from [15]. CC BY 4.0.

peak-to-peak amplitude is 16 mm and has a spectral resolution of ≈ 5 GHz. The interferogram is measured by an active cooled InSb-detector. It can be expressed by:

$$I(x) = \int_0^\infty W(k)\cos(2\pi k x)d\,k \tag{3.1}$$

where k denotes the wave number, x the optical path difference in the arms of the interferometer and $W(k)$ the radiation from the plasma. Applying the reversed Fourier Transform yields the spectrum of the radiation. Mechanical constraints of the sweep time of the mirror determine the temporal resolution of the instrument to ≈ 22 ms. For the purpose of a hot-cold calibration, two black body sources at liquid Nitrogen temperature and at 600 deg Celsius are used. Due to the attenuation on the long transmission line, the calibration of the instrument applying coherent averaging takes 40 min to improve the signal-to-noise ratio. Furthermore, the ECRH-injection at $f = 140$ GHz needs the installation of a notch filter to protect the instrument against stray radiation. Due to the large attenuation, the Michelson is operated with a multimode input. A notch filter is therefore assembled by multilayer dielectric structures. However, the width of the notch is approximately 10 GHz [14] wide and perturbs the profile measurement. Reducing the number of transmitted modes will allow the use of a standard, wave guide based notch filter on the expenses of reduced power. Furthermore, the operation at high densities requires ECRH-heating at O2 and X3 heating. In this case, a single path absorption of the ECRH-power is no longer possible and the stray radiation increases. This must be effectively removed to allow a meaningful measurement.

The main purpose of the Michelson interferometer is the measurement of the radiation temperature in cases where the local density overcomes the cut-off frequency for the 2nd harmonic ECE-radiation. An example of the measured radiation temperature (T_{rad}) spectrum for different plasma density is shown in figure 2a. It demonstrates clearly the effect of the increase of the cut-off frequency with density, leading to a strong decrease in T_{rad} for the X2-mode radiation. At the same time, the X3-mode is increasing and becoming optical thick. Also, the comparison of the electron temperature (T_e) estimated by the Michelson interferometer with the ECE-radiometers is performed. In figure 2b the comparison between the radiometer and the Michelson interferometer is shown within the flat top phase for two discharge with similar plasma parameters. Since both instruments share the same beam-line, propagation effect in the transmission line can be neglected and a good agreement for

2025 JINST 20 C12008

the frequency range 135 GHz to 150 GHz is achieved, corresponding to the plasma core and the high field side. The less agreement for $f \leq 134$ GHz has its possible origin in the uncertainty of calibration at lower frequencies of the Michelson. Within the upcoming campaign, the front end of

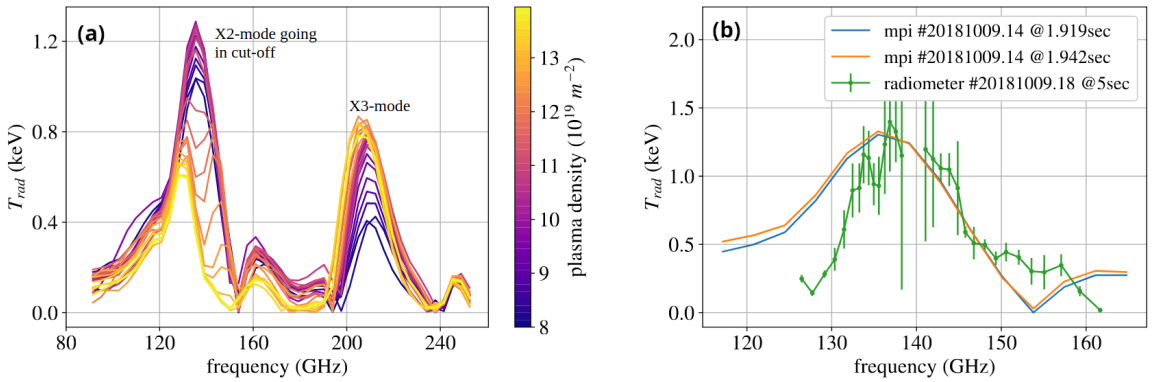

Figure 2. (*a*): measurement of T_{rad} for 2$^{\mathrm{nd}}$- and 2$^{\mathrm{nd}}$-harmonic X-mode, demonstrating the cut-off effect for increasing density in the 2$^{\mathrm{nd}}$-harmonic. (*b*): the comparison of T_{rad} estimated from Michelson and ECE-radiometers, showing a good agreement. Reproduced from [11]. The Author(s). CC BY 4.0.

the Michelson interferometer will be improved by a new designed quasi-optical polarization tuner designed by the Stuttgart University [16] and the attenuation of the beam-line is going to be decreased by separating the Michelson from the radiometers.

3.2 Heterodyne radiometry

The heterodyne radiometry at W7-X is designed for an operation at a magnetic field of $B_t = 2.5$ T [17]. It makes use of the 2$^{\mathrm{nd}}$ harmonic X-mode and covers the frequency range 126 GHz to 162 GHz with a total of 32 channels. It shares the Gaussian telescope and the transmission line in vacuum with the Michelson interferometer. The radiation from the plasma passes a vacuum window consisting of a 100 µm mica window sealed by a Viton ring. The copper wave guide has a circular cross-section with a diameter of d=28 mm. Before the notch filter, the wave guide is tapered down to a diameter d=4 mm. Due to the restricted frequency range of 126 GHz to 162 GHz, a Bragg reflection notch filter [20] is applied, yielding a notch depth of 40 dB for the ECRH stray radiation window from 139.9 GHz to 140.4 GHz. The total transmission line losses sum up from 8 dB to 10 dB along the path length of 23.7 m.

The radiometer (see figure 3) consists of a PLL stabilized local oscillator at f=122 GHz and an ultra-wideband mixer with an integrated diplexer. The intermediate frequency range (IF) of 2 GHz to 40 GHz is split over two filter banks of 2 GHz to 18 GHz and 18 GHz to 40 GHz width. Each individual filter is designed to keep the radial resolution in the range of 0.5 cm to 1 cm. The bandwidth of the individual filters ranges from a minimum of 0.25 GHz for the low field side ECE channels to up to 1.4 GHz for the high field side ECE-channels. This is necessary because the HFS channels are less sensitive. Each of these channels after detection by a diode and preamplification is adapted by remote controlled backend amplifiers and digitized at a sampling rate 2 MS/s. This sampling rate allows studying fast events, e.g. sawtooth crashes and pellet-injection, in detail. In addition to the two standard filter banks, a third one is operated in parallel. This so-called "ZOOM"-device [18, 19] consists of a second down conversion step with a tuneable local oscillator and yields a range of intermediate frequencies (IF) of 20 GHz to 24 GHz. The tuneable oscillator allows shifting the investigated region

2025 JINST 20 C12008

across the plasma diameter. Each filter has a bandwidth of 150 MHz. The "ZOOM"-device provides additional 16 channels, which correspond to a radial range of $\Delta r = 6$ cm on the high field (HFS) and $\Delta r = 14$ cm on the low field side (LFS). For the estimation of a Te-profile from the measured calibrated radiometer spectra, the plasma equilibrium using VMEC [21] along the ECE sight line and the density profile from Thomson scattering are needed to run radiation transport calculations via the TRAVIS code [22]. A result is shown in figure 4, where each data point corresponds to one radiometer channel. As can be seen, the emission in the plasma centre is close to blackbody radiation with a high degree of localization. Channels at the LFS, displayed by negative values of ρ in this figure, are affected strongly by red shifted radiation from the hot plasma core. It causes an inward shift and a large error in the radial localization in figure 4.

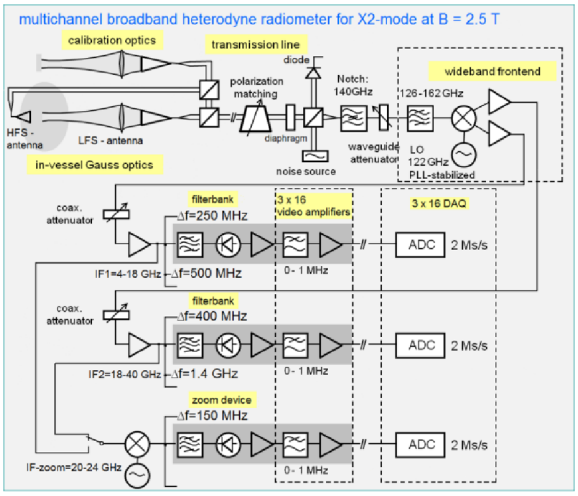

Figure 3. Schematic view of the 32-channel radiometer as it is used at W7-X. Note the 16-channel "ZOOM"-device at the bottom. Reproduced from [17]. CC BY 4.0.

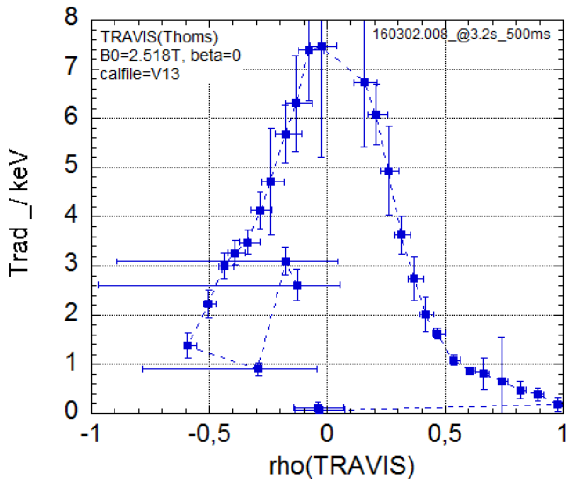

Figure 4. Electron temperature profile as function of ρ as calculated from the ECE diagnostic with TRAVIS- and VMEC-calculations. Reproduced from [17]. CC BY 4.0.

As mentioned in section 1, W7-X is a device for high density operation, since there is no driven current related Greenwald density limit. In the first campaigns, beside the Thomson Scattering diagnostic, only the Michelson interferometer was able to provide T_e-profiles in case the X2-radiation was in cut-off. Such conditions often happen, when high-β-plasmas are achieved by increasing the plasma density. However, due to the coarse time resolution, an X3-radiometer is necessary to monitor the fast evolution of the electron temperature in the core and on the LFS, as it happens e.g. in pellet injection events. For this purpose, a 16 channel radiometer operating in G-band was designed and constructed. The schematic view of the instrument is shown in figure 5. The radiometer is connected to the same Gaussian telescope where the X2-radiomter is installed. A power divider is used to split the input power towards the X2- and X3-radiometer. The frequency range covers 200 GHz to 232 GHz covering the whole 3rd-harmonic as can be seen in figure 2. The local oscillator at $f = 96$ GHz after a multiplying the frequency by a factor 2 is feeding a mixer together with the radiation from the plasma. It delivers an IF in the range of 1 GHz to 35 GHz. A part of the IF-signal from the mixer is down converted in a second step and feeding a filter bank with 8 channels. This down conversion step is necessary, because the efficiency of detector diodes is reduced for $f \geq 18$ GHz. The other half of the

2025 JINST 20 C12008

IF-signal is separated via a two-way and four-way power divider. Each part feeds a filter bank. The range of the filter width is increasing, yielding an increase of the radial resolution of the HFS. As for the X2-radiometer, the signal after the video amplifier chain is sampled with up to 2 MS/s.

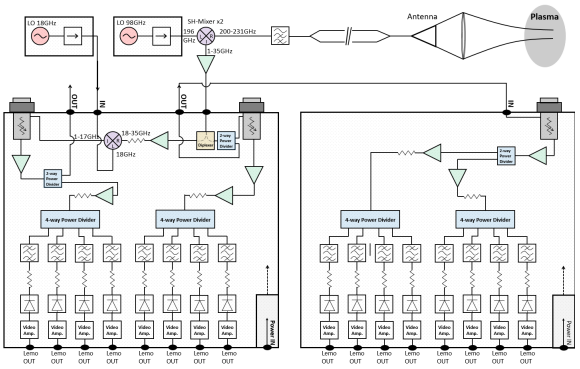

Figure 5. Schematic view of the 16-channel radiometer for the measurement of 3rd-radiation as it is used at W7-X.

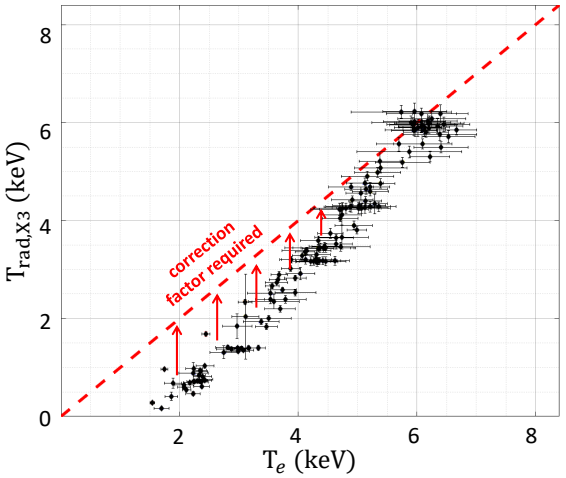

Figure 6. Comparison of X3 radiation temperature versus T_e from TS, demonstrating the influence of the optical depth on the measurement. Reproduced with permission from [23].

Within the last campaign, a comparison between T_e-signal from Thomson scattering (TS) with the X3-radiometer is performed. Whereas, the temporal evolution of the core temperature is well described, the absolute temperature deviates from the one obtained by TS (see figure 6). The correction factor reduces significantly in case of high T_{rad}, indicating the large impact of the electron temperature on the optical depth.

Comparing T_e from TS with X2- and X3-radiometer shows, across campaigns, a 10 % to 15 % smaller T_e from X2 compared to TS. Further analysis is ongoing, including an intermachine comparison with the hypothesis that non-thermal particles will perturb the Maxwellian distribution [24].

The X3-radiation is also used as an interlock for the density control [23]. The control circuit detects if the T_e falls below a certain threshold. In case this condition is fulfilled, the gas valve is closed. This control was already tested for X2-radiation but, is available since OP2.3 for X3-radiation, too.

3.3 Correlation ECE

The purpose of correlation ECE (CECE) is the measurement of coherent and broadband turbulence across the minor radius of W7-X. In the first campaigns at W7-X the 16-channel "ZOOM"-device was used to measure T_e-fluctuations. With the 150 MHz bandwidth of each individual channel, the system is used to measuring radial correlations in a wave number (k_r) range of 0.3 cm^{-1} to 5 cm^{-1}. The "ZOOM"-device is capable to measure temperature fluctuation down to 0.3 % [25]. In the first campaigns, a coherent mode ranging from 7 kHz to 10 kHz was observed near the location of the 4/5 non-resonant surface in the standard configuration.

Beginning with the campaign OP2.1, a radial correlation ECE (CECE) has started its operation [28]. It is located near to symmetric planes with a bean shaped polidal plasma cross-section. The sophisticated

2025 JINST 20 C12008

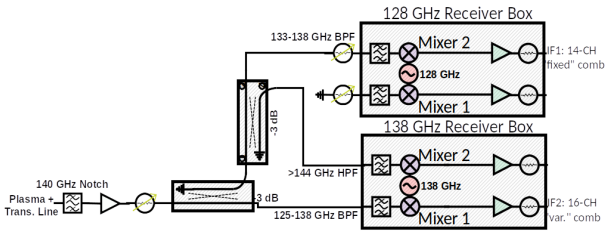

Figure 7. Schematic view of the first mixing stage of the CECE-system at W7-X, showing the splitting of the signals in an LFS and HFS branch. Reproduced with permission from [28].

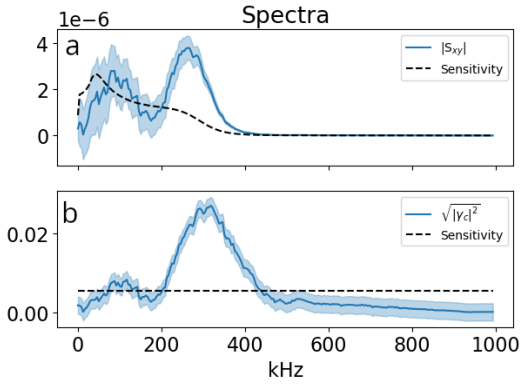

Figure 8. (*a*) Cross spectrum for two ECE-channels and (*b*) Coherence spectrum, showing the broad structure at $f \approx 250\,\mathrm{kHz}$.

system has its own dedicated and optimized antennae, followed by an oversized transmission line. The radiation is filtered for LFS- and HFS-frequencies separately and feeds two receiver boxes (see figure 7), with a first mixing stage. In a further down conversion step, a radial scanning comb is generated. For this down conversion step a remotely controlled synthesizer as local oscillator is used similar to the "ZOOM"-device described in section 3.2. It allows shifting the investigated frequency interval along the minor radius. After passing a filter bank, 16 frequency channels are provided on the LFS and HFS, separately, each having a bandwidth of 150 MHz. As an example of the CECE, the cross- and coherence-spectra are shown in figure 8. The spectra are obtained from two ECE-channels at $f = 130.4\,\mathrm{GHz}$ and $f = 130.8\,\mathrm{GHz}$. They are located at a radial position of $r/a = 0.7$. The dashed line in each spectrum displays the sensitivity of the diagnostic. A clear indication for a broad mode structure, centred at $f \approx 250\,\mathrm{kHz}$ is found. This broad structure has been observed by a poloidal correlation reflectometer (see section 4.2) and is identified as ∇T_e-driven trapped electron mode.

Instead of correlating nearby frequencies, it is also possible to correlate the same frequency interval with itself, but, adding a delay [26]. The delay must fulfil the following requirements, (i) it should be long enough to suppress thermal noise and (ii) short enough to catch T_e-fluctuations. The thermal noise depends on the bandwidth of the video amplifier (B_{vid}) and the half width can be described by $t_{1/2} = \sqrt{ln\ 2/\pi}/B_{\mathrm{vid}}$. The schematic view of a time delay CECE is shown in figure 9. For this application, the intermediate frequency of the frequency CECE-system is used. This signal passes a power divider and one half of the IF-power is passing an additional delay line before being detected in the same way and, as demonstrated in the last campaign, with a delay of 160 ns corresponding to 5 $t_{1/2}$ some first measurements are obtained and the analysis has been started.

3.4 Imaging ECE

A correlation ECE-Imaging system (cECEI) is envisaged for the OP2.6 campaign of W7-X starting early summer 2028. It is planned to have an overlap with the Heavy Ion Beam Probe (HIBP) which is proposed for turbulent electron heat flux studies. As for every ECEI system, the installation needs large port access for the optical components. Three different optical systems have been proposed [27]. At the moment, tests are ongoing to develop a compact focusing optical system at W7-X [28].

2025 JINST 20 C12008

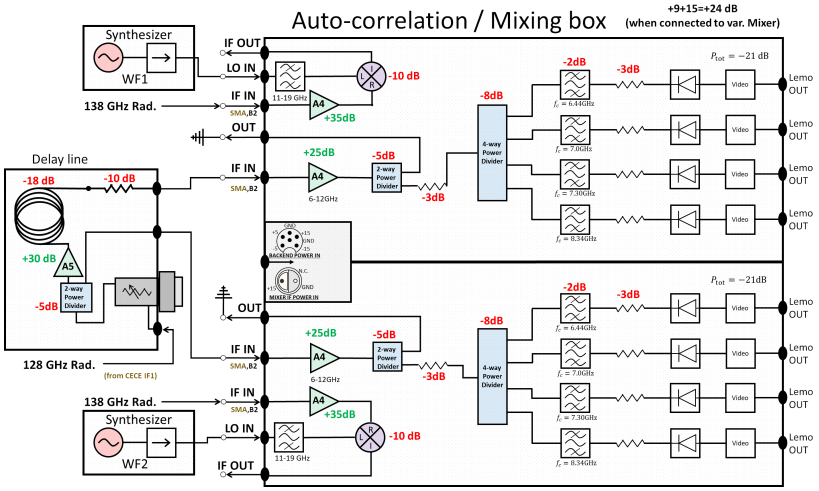

Figure 9. The set-up of the delay time CECE-system. The delay is added after the first mixing stage. In total, 8 fixed frequency channels are realized. Reproduced with permission from [28].

4 Active microwave diagnostics

This section will describe active microwave diagnostic, making use of eqs. (2.2) and (2.4). The active diagnostics consists of several Doppler reflectomter (DR), a poloidal correlation reflectometer (PCR) and a density profile reflectometer (DPR). The first two (DR and PCR) provide profiles of the poloidal rotation of the main plasma and the turbulence. Once the rotation is estimated, the radial electric field (E_r) can be deduced, an important quantity for the radial neoclassical transport. With different injection angles, the DR can also investigate turbulence at different wave numbers. Furthermore, PCR can deliver poloidal correlation length and turbulence spectra. The DPR is mainly installed for measuring the electron density profile in front of the ICRH antenna to improve the coupling of the ICRH power to the plasma. A Collective Thomson Scattering (CTS) diagnostic is installed to measure the ion temperature (T_i) of hydrogen in the plasma. Furthermore, it allows getting information on fast particles in the plasma

4.1 Doppler reflectometry

A Doppler reflectometer is an instrument that measures the frequency shift (Doppler shift) of reflected waves from a moving target rough surface. A DR-system which measures the backscattered power of a launched microwave at an oblique angle at the -1^{st} order of reflection is a monostatic system and is called a Doppler backscattering system (DBS). Already in the first campaign of W7-X, a DBS has been installed for the measurement of the poloidal plasma flow and the related radial electric field (E_r) [29, 30]. Such a set-up is sensitive to different wave number ($k_\perp$) values depending on the poloidal tilt angle. Selecting the tilt angle (θ_{tilt}) of the antenna allows measuring structures of a certain $k_\perp$. The relation between the measured wave number and the tilt angle is given by $k_\perp = 2k_0 \sin(\theta_{\text{tilt}})$, where k_0 denotes the wave number of the probing frequency.

In total, 4 DBS-systems at two distinct toroidal locations are in operation at W7-X, three of them at one of the bean shaped poloidal cross-section. The V-band (50 GHz to 75 GHz) and the E-band (60 GHz to 90 GHz) DBS-systems are operated in O-mode polarization and at a fixed steering angle of $\theta_{\text{tilt}} = 18°$, corresponding to wave numbers of 7 cm^{-1} to 14 cm^{-1}, see figure 10 AEA21-B. The set

2025 JINST 20 C12008

of DBS-systems at this position is completed by a W-band DR in the frequency range of 75 GHz to 110 GHz. It has a steerable mirror from −20° to 5° which allows measuring a wave numbers in a range of $-20\,\mathrm{cm}^{-1}$ to $5\,\mathrm{cm}^{-1}$ (figure 10 AEA21-U). The two O-mode DBS-systems are connected two a Gaussian telescope with 3 focusing mirrors. The X-mode system is connected to a similar Gaussian telescope, where the last mirror is steerable. A fourth DBS-system is installed at $\phi = 229°$ for V-band (50 GHz to 75 GHz) covering a density range of $2.8 \times 10^{19}\,\mathrm{m}^{-3}$ to $6.3 \times 10^{19}\,\mathrm{m}^{-3}$. It is equipped with a steerable mirror in the range −20° to 5° covering a wave number range of $-10\,\mathrm{cm}^{-1} \leq k_\perp \leq 10\,\mathrm{cm}^{-1}$. Together with the DBS-system at $\phi = 72°$ it is mainly used to measure toroidal long range correlations as needed for the verification of zonal flows in W7-X. Due to the partial frequency overlap of the

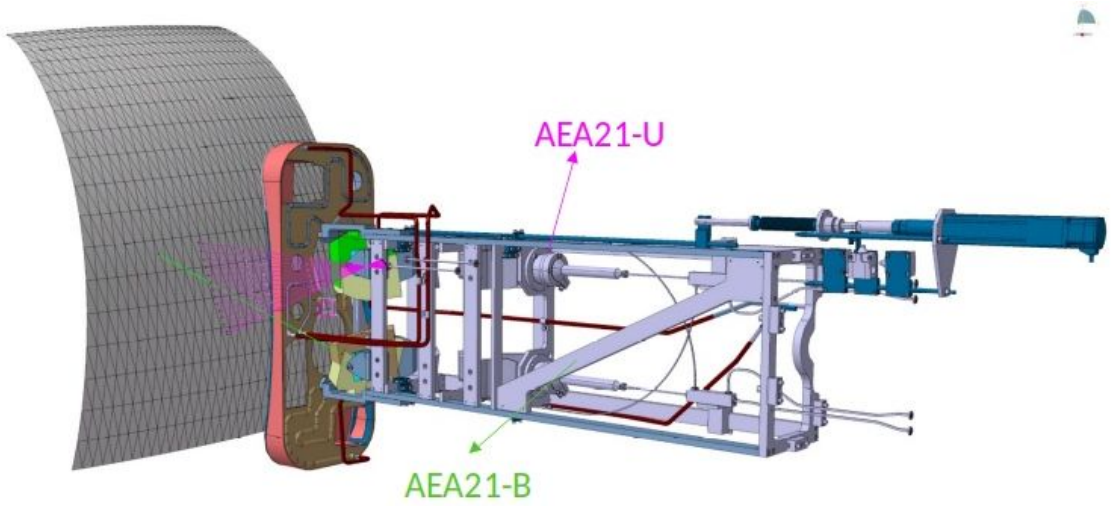

Figure 10. The DBS installation in the AEA21-port, viewing the bean-shaped plasma cross-section with the two Gaussian telescopes for the O-mode and X-mode DBS systems. Reproduced with permission from [31].

V-band and E-band DBS, the measurement of radial correlation in a 15 GHz broad frequency range is possible. All DBS systems are hopping reflectometers with heterodyne IQ-detection, utilizing a frequency step of 0.5 GHz and a plateau interval of 30 ms in general, I/Q-signals are measured at a rate of 20 MHz. From the measured Doppler spectrum, the frequency shift is determined. The four DBS-systems can be combined in a way that either long range correlations are measured between the V-band systems or radial correlations between the V-band and the E-band system are measured due to the frequency overlap in the two bands. Radial correlations are measured at one toroidal position and also by using the V-band DBS at the 2nd toroidal position.

The measurements of the DBS-systems have contributed to the understanding of the impact of the 5/5-island at the vicinity of the last close flux surface [32]. It could be shown that the $E \times B$-flow achieves a maximum at the island boundaries and is close to zero at the island O-point. Also, the reduction of density fluctuations in the post-pellet phase with improved confinement properties was shown [33]. Cross different magnetic configurations, E_r and the velocity shear was studied as function of heating power and density. A good agreement between the experimental results and neoclassical predictions is achieved [34]. In the scrape-off layer (SOL), the relation between the E_r in the SOL and the divertor heat flux is studied, showing that the E_r depends on parameters of the divertor [35].

2025 JINST 20 C12008

In a paper on microwave diagnostic at W7-X another W-band DR-system should not be missed. It was operated during the first two campaigns. As mentioned above, $k_\perp$ depends on the tilt angle of the launched microwave beam. Tilting the microwave beam can be done by a motor as for the W-band DBS described above or by using a phased array antenna (PAA). A PAA allows beam shaping and side lope suppression [36] and consist of a helical delay in fundamental wave guide. It has one coupling element on each of the turns (see figure 11a,b). This feed network is combined with a sectoral horn antenna. However, the coupled power to the antenna array is quite small (−15 dB). Sweeping

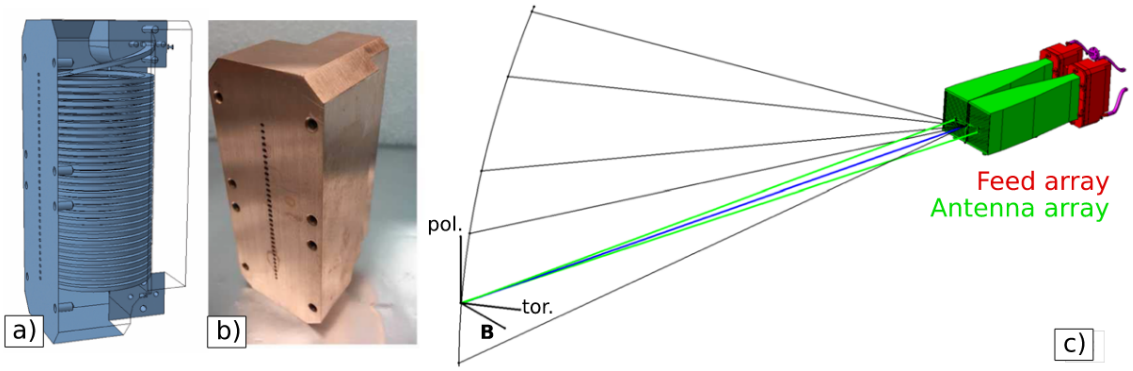

Figure 11. (*a*) CAD figure of the PAA and (*b*) the electroformed feed array. (*c*) CAD model of the bistatic DR set-up. Reprinted from [37], with the permission of AIP Publishing.

the frequency slowly, will change the tilt angle and the measured $k_\perp$. Such an PAA was designed and developed [38] and installed at W7-X at a toroidal position of $\phi = 71°$ and 140 mm above the midplane. The DR-system is a bistatic system, using two PAAs, one for the launching part and one for the receiving part. In figure 12a the dependence of the tilt angle from the frequency is shown for the transmitting and receiving PAA. For a narrow frequency interval of $\Delta f \approx 1$ GHz a tilt angle range from −40° to 20° is achieved. The corresponding pattern for a sweep at $f_c = 104.23$ GHz is shown in figure 12b. It demonstrates that a reasonable signal strength can be realized for $-20° \leq \theta \leq 20$ degree.

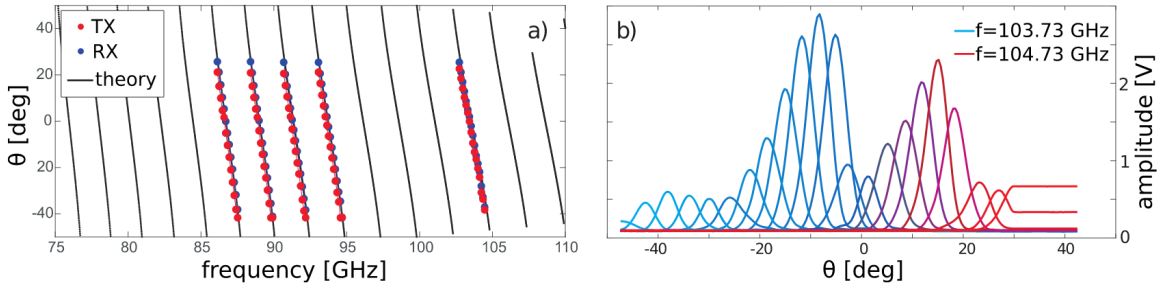

Figure 12. (*a*) Relation between frequency and tilt angle. (*b*) Strength of the antenna pattern as function of the used frequency. The frequency is colour coded. Reprinted from [37], with the permission of AIP Publishing.

4.2 Poloidal Correlation Reflectometry

Poloidal Correlation Reflectometry (PCR) is a diagnostic technique used to measure turbulence and plasma fluctuations in the poloidal direction. It works by analysing the correlation between signals from two or more antennas located at two poloidally shifted locations. The signals are generated by the

2025 JINST 20 C12008

reflection of a launched microwave at the cut-off layer. By studying the temporal and spatial coherence of these signals, PCR provides insights into the structure and dynamics of plasma turbulence, which is crucial for understanding transport processes in tokamaks and stellarators. This method is particularly useful for investigating low-frequency, long-wavelength fluctuations that affect plasma confinement.

At W7-X the PCR [39, 40] is operated in O-mode polarization and uses heterodyne I/Q-detection. It is located in the same plasma cross-section as the DBS-systems. The antenna head is located below the midplane and looking upwards to a common focal point at $R = 6.0\,\mathrm{m}$ and $z = -0.104\,\mathrm{m}$. The PCR consists of a single antenna to launch the microwave beam and a set of four receiving ones viewing four different poloidally separated reflection areas. All antennae are aligned perpendicular to the magnetic field line. In figure 13b the antenna head of the PCR-system is shown. The single lines of sight are displayed by red lines. The antenna head is embedded in a copper structure, which is water cooled to withstand the temperature increase during long pulse operation. The launching antenna is the middle one in the left row. The antennae are connected via waveguides (WR28) with the reflectometer, which is located in the torus hall. The system is operated in two frequency bands, (i) the Ka-band, 23 GHz to 40 GHz available with the beginning of the operation of W7-X and (ii) the U-band 40 GHz to 60 GHz which became available with the start of the campaign OP2.1. It allows measuring reflected signals up to a cut-off layer density of $n_e = 4.5 \times 10^{19}\,\mathrm{m}^{-3}$. With respect to wave-numbers, the PCR system is

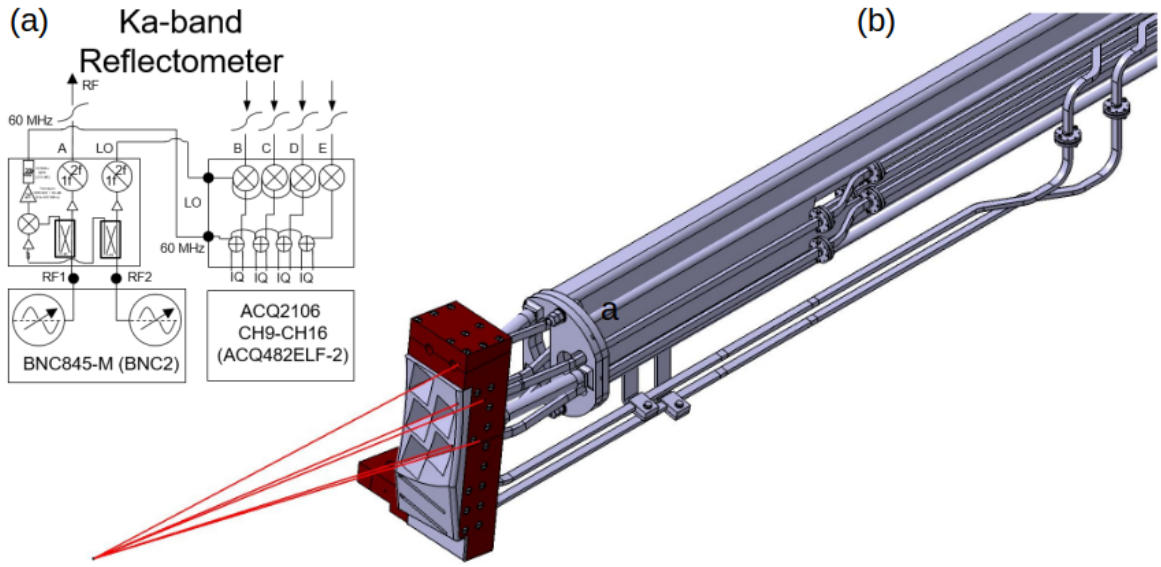

Figure 13. (*a*) Electronic scheme of the Ka-band PCR. (*b*) CAD-view of the PCR plugin with the 5 horn antennae, surrounded by a copper cooling block.

sensitive to a $k_\perp \leq 3.0\,\mathrm{cm}^{-1}$ [41, 42], due to its nearly perpendicular incidence. The electronic scheme of the PCR is shown in figure 13a. From the 4 receiving antenna, the I/Q-signals from 6 combinations are measured at a sampling rate of 5 Ms/s. The cross correlation of the complex time series from each antenna combination, yields the delay time resulting from the poloidal propagation of the turbulent structures and with the knowledge of the poloidal separation on the probed flux surface, the velocity of the turbulence at the cut-off layer for 6 different poloidal distances is estimated. The PCR is operated in a frequency hopping regime. Frequency steps and duration are variable and programmable, but, in the most cases, a frequency step of 0.5 GHz for a duration of 10 ms is used in poloidal correlation

2025 JINST 20 C12008

measurements. The flexible programming of the PCR allows the measurement of radial correlations at the frequency limits ($f \approx 40\,\mathrm{GHz}$) of both bands. In this case, the frequency separation between the Ka- and U-band system is $\Delta f \approx 100\,\mathrm{MHz}$ due to the small radial correlation length of the turbulence.

Due to the high density operation in the majority of plasma in OP2.2 and OP2.3, a further upgrade by an extension to the E-band, 60 GHz to 90 GHz, is planned for the next campaign, allowing the measurement of turbulence properties up to $n_e \approx 1.0 \times 10^{20}\,\mathrm{m}^{-3}$.

The PCR-system complements the DBS-systems towards the low wave-number turbulence, The system is capable to measure the time delay for a given combination for different frequency intervals and allows separating the time delay of the main $E \times B$ plasma flow from the one generated by broad band quasi coherent modes. From the estimated time delay and the turbulence velocity is deduced by applying the elliptical model [43, 44]. Modes are observed across a large frequency range and magnetic configurations. Broad quasi coherent (QC) modes are observed with a central frequency of $f \geq 100\,\mathrm{kHz}$ in the plasma core, having a scale of, $k_\perp \rho_s \geq 1.0$. They are identified as ∇T_e driven trapped electron modes [45]. Also in the SOL, a narrow quasi coherent mode is investigated with decreasing frequency from 25 kHz to 10 kHz when the cut-off layer is moving towards the plasma core [46], having a normalized mode scale of $k_\perp \rho_s \leq 0.1$. Another low frequency mode in the range 1 kHz to 2 kHz modulating the plasm flow is observed in the SOL [47]. The influence of the magnetic topology in the plasma edge on the shear layer is investigated, and it could be demonstrated that broad band turbulence is suppressed in the shear layer [48].

4.3 Density-profile reflectomery at the ICRH-antenna

For the determination of the electron density in front of the ICRH-antenna [49] a frequency modulated continuous wave (FMCW) reflectometer [50–52] is installed in the ICRH-antenna at a toroidal angle of 153°. The long term goal is the determination and control of the local electron density in front of the antenna. The reflectometer can be operated independently of the ICRH operation, allowing to measure edge density profiles in all plasma scenarios. Due to its localization in the ICRH antenna, a measurement in the core plasma is not possible, but the gradient region is fully covered. The reflectometer is mounted on the same movable trolley as the ICRH antenna, allowing for a radial propagation of 0.3 m. The installation on the trolley keeps the transmission line short and avoids the use of flexible wave guides. Within the ICRH antenna, two pairs of sectoral Ka-band antenna are mounted as shown in figure 14a in blue colour, allowing for X-mode launch. The transmission line consist of WR28 wave guides in the vacuum section. Outside the vacuum section, the transmission line is made of fundamental wave guides (WR10 and WR12) for W- and E-band. The reflectometer consist of two bands, the E-band and the W-band. The linearity of the output frequency for both frequency ramps as function of the VCO-voltage is shown in figure 14c before multiplying by a factor 6 and 8, respectively. With both bands, a density range from $0.2 \times 10^{19}\,\mathrm{m}^{-3}$ to $6.4 \times 10^{19}\,\mathrm{m}^{-3}$ is accessible. An outline of the microwave circuit is shown in figure 14b. The output signal of a voltage tuneable oscillator (VCO) is modulated, multiplied in frequency and launched into the plasma. The reflected signal is mixed with a reference signal which, for better comparison, is delayed by the same time the reflected signal needs to propagate to the antenna and back. The principle of a density profile reflectometer is to sweep the microwave frequency over a full band in a time equivalent or faster than the lifetime of turbulence structures in the plasma, to keep the density profile as frozen with respect to turbulence. This asks for a high sampling rate of $\geq 10\,\mathrm{MHz}$. From the spectrogram of

2025 JINST 20 C12008

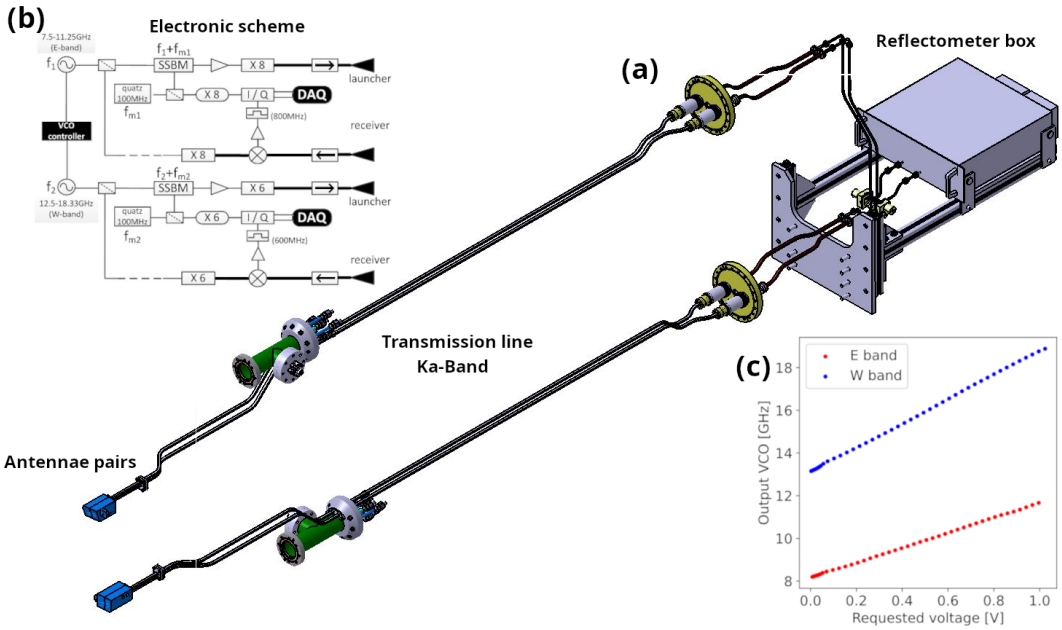

Figure 14. Schematic view of the installation of the reflectometer within the ICRH antenna. Clearly see are the two pairs of antennae, the long transmission line in the vacuum and density profile reflectometer back end.

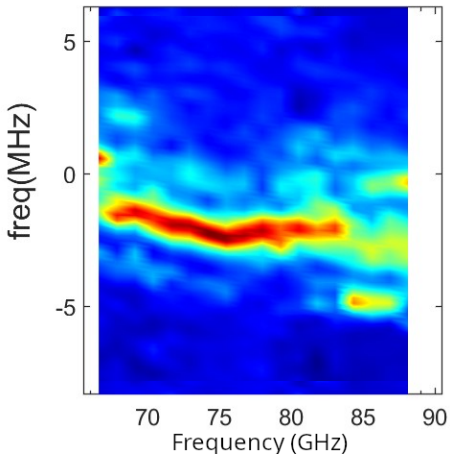

Figure 15. Spectrogram of the beat frequency, showing the change of the beat frequency with probing frequency.

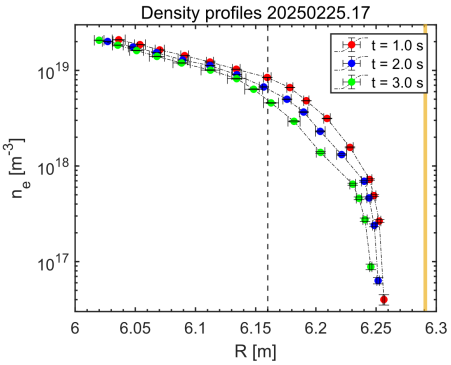

Figure 16. Density profiles for three different time stamps. The profile at $t = 3\,\mathrm{s}$ is obtained during ICRH operation. The dashed line indicates the LCFS.

the complex signal the beat frequency f_{beat}, defined as

$$f_{\mathrm{beat}}(t) = \tau_d(t)\frac{dF}{dt} \tag{4.1}$$

is calculated, with τ_g being the group delay and dF/dt the sweep rate. An example of the beat frequency spectrogram is shown in figure 15, which shows clearly the change of the beat frequency with the probing frequency. The group delay is a measure of the distance travelled by the probing

2025 JINST 20 C12008

frequency and yields a density profile. Recent measurements of density profiles during the ICRH operation are shown in figure 16, where the profiles at $t = 1\,\mathrm{s}$ and $t = 2\,\mathrm{s}$ are measured without ICRH operation and the profile at $t = 3\,\mathrm{s}$ is obtained for an ICRH pulse of $P_{\mathrm{ICRH}} = 500\,\mathrm{kW}$. A clear change in the profile is observed outside the LCFS in the SOL.

4.4 Collective Thomson scattering

Instead of measuring the scattering from individual free electrons, CTS measures the scattered signal from correlated density fluctuations. Therefore, the wave vector k must fulfil the condition $k \lesssim 1/\lambda_D$, where λ_D denotes the Debye-length. Instead of using a laser, a microwave beam is used as probing radiation. Microwave based CTS has proven its capability in many fusion devices to determine the bulk ion temperature (T_i), ion composition and flow velocity from the analysis of the scattered

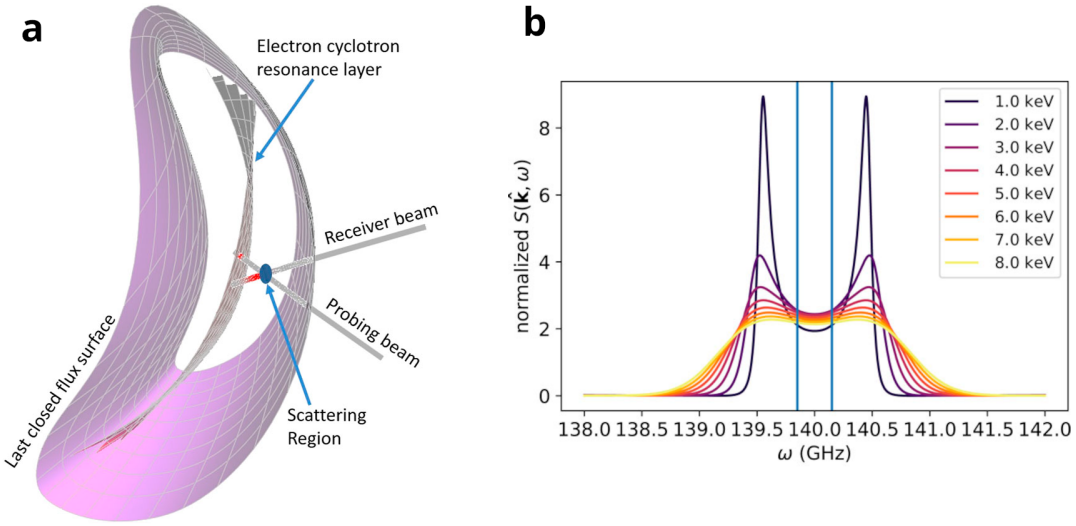

Figure 17. (*a*) Schematic view of the scatter geometry at W7-X. (*b*) Influence of the ion temperature on the spectral shape of the scattered radiation. Reprinted from [53], with the permission of AIP Publishing.

radiation. The principle of a CTS-system is shown in figure 17a with the probing and receiving beam. Fluctuations are measure along $k_\delta = k_r - k_p$ with k_P and k_R denoting the probing and receiving wave vectors. The spectral shape depends on the scatter geometry (known) and plasma parameters. In figure 17b the influence of T_i on the spectral shape is shown, calculated by the developed forward model (eCTS). It calculates the spectral power density of the scattered radiation. The spectral analysis is performed with function parametrization or with an artificial neural network. At W7-X a neural network analysis is applied for a fast determination of the T_i [53]. The CTS-system at W7-X [54] uses 2 gyrotrons from the ECRH-system at two different nearby toroidal positions with frequency of $f = 140\,\mathrm{GHz}$. One spare ECRH-launcher is used as front-end receiver antenna. Two different toroidal positions are investigated, (i) in the bean shaped plasma cross-section, where a set of steerable mirrors allows scanning the range of k_δ angles from 85° to 120° and (ii) the triangular cross-section, which allows for a scatter volume in the plasma centre. Due to the topology of the magnetic field, better resolution of T_i measurements in the magnetic flux co-ordinates can be achieved in the triangular cross-section. Also, the cold resonance at 140 GHz does not allow a placement of the scatter volume in the very core. The CTS receiver consists of a heterodyne radiometer equipped with a 16 channel filter

2025 JINST 20 C12008

bank in the range 135 GHz to 145 GHz. First measurements with the CTS-system at both positions show a good agreement of the measured T_i with the one from X-ray spectroscopy.

Due to the gyrotron operation at 140 GHz the measurement of T_i needs long averaging times to deal with the poor signal-to-noise ratio coming from the strong electron cyclotron emission. This can be avoided by using another gyrotron frequency which is not for plasma heating. Constraints in the vacuum window for the ECRH as well as decoupling a reasonable amount of power from the existing gyrotrons asks for a probing frequency of 175 GHz [55, 56]. The selection of this frequency comes along with the potential risk that microwave diagnostics are not equipped with notch filters for this frequency. This has to be changed in the upcoming campaigns. A change of the probing frequency comes along with an upgrade of the CTS receiver for the new frequency. Because the CTS should be operated at both probing frequencies 140 GHz and, 175 GHz a dual frequency horn is installed followed by a waveguide switch to direct the scattered radiation to the appropriate radiometer. The 174 GHz CTS-system is in operation since the campaign OP2.1. Due to the reduced width of the notch filter and improved signal-to-noise ratio, the time for one normalized spectrum from which T_i is estimated is reduced to 3 ms. With this good temporal resolution it is possible to follow even fast events in the plasma.

Beside the measurement of the ion temperature, CTS is used to detect fast ions, as they are generated by the neutral beam injectors (NBI) at W7-X. When comparing the power spectral density at time intervals with and without NBI. The spectra consist of three components, the ECE, the thermal NBI and the fast ion component [57].

5 Summary

The paper aims in giving an overview of the installed and foreseen microwave diagnostic at W7-X. It describes the important frequencies in the propagation of microwaves in plasmas in terms of resonances and cut-offs, and shows how they are used in the estimation of physical quantities as temperatures of plasma species profiles, plasma rotation profiles and turbulence properties. Beside the technical outline of the discussed microwave diagnostic, also an overview of recently achieved results is included. Active and passive microwave diagnostics are discussed, as reflectometry, collective scattering and electron cyclotron emission. The deployment of microwave diagnostic is important due to reduced requirements on mirrors and calibration compared to other optical diagnostics. This advantage makes microwave diagnostic interesting for application in the harsh environment of future fusion devices.

Microwave diagnostics are valuable tools in fusion research because they provide accurate, non-intrusive measurements of essential plasma parameters, enabling researchers to better understand and control the fusion process.

Acknowledgments

This work has been carried out within the framework of the EUROfusion Consortium, funded by the European Union via the Euratom Research and Training Programme (Grant Agreement No 101052200 –EUROfusion). Views and opinions expressed are however those of the author(s) only and do not necessarily reflect those of the European Union or the European Commission. Neither the European Union nor the European Commission can be held responsible for them.

2025 JINST 20 C12008

References

[1] B. Vowinkel, *Passive Mikrowellenradiometrie*, Vieweg (1989).

[2] H.J. Hartfuß and T. Geist, *Fusion Plasma Diagnostic with mm-Waves*, Wiley VCH (2013) [DOI:10.1002/9783527676279].

[3] T. Klinger et al., *Performance and properties of the first plasmas of Wendelstein 7-X*, *Plasma Phys. Control. Fusion* **59** (2016) 014018.

[4] R.C. Wolf et al., *Major results from the first plasma campaign of the Wendelstein 7-X stellarator*, *Nucl. Fusion* **57** (2017) 102020.

[5] J. Geiger et al., *Physics in the magnetic configuration space of W7-X*, *Plasma Phys. Control. Fusion* **57** (2014) 014004.

[6] V. Erckmann et al., *Electron Cyclotron Heating for W7-X: Physics and Technology*, *Fusion Sci. Technol.* **52** (2007) 291.

[7] M. Bornatici, R. Cano, O. De Barbieri and F. Engelmann, *Electron cyclotron emission and absorption in fusion plasmas*, *Nucl. Fusion* **23** (1983) 1153.

[8] I.H. Hutchinson, *Principles of Plasma Diagnostics: Second Edition*, *Plasma Phys. Control. Fusion* **44** (2002) 2603.

[9] A. Krämer-Flecken and P.C. de Vries, *Measurement of 3rd Harmonic of ECE-Radiation at TEXTOR-94* in the proceedings of the *10*th *Workshop of ECE and ECRH*, Ameland, Netherlands, World Scientific, Singnapore (1997) 209.

[10] J.W. Oosterbeek et al., *Michelson Interferometer design in ECW heated plasmas and initial results*, *Fusion Eng. Des.* **146** (2019) 959.

[11] N. Chaudhary et al., *Investigation of higher harmonics of electron cyclotron emission using Fourier transform spectroscopy in Wendelstein 7-X*, 2020 *JINST* **15** P09024.

[12] N. Chaudhary, *Investigation of optically grey electron cyclotron harmonics in Wendelstein 7-X*, Technische Universität Berlin, Germany (2021) [DOI:10.14279/depositonce-12630].

[13] B. Plaum, *Optimization of Broadband Smooth-Wall Circular Horn Antennas*, *J. Infrared Milli. Terahz. Waves* **39** (2018) 984.

[14] N. Chaudhary et al., *Investigation of Optically Grey Electron Cyclotron Harmonics in Wendelstein 7-X*, *EPJ Web Conf.* **203** (2019) 03005.

[15] J.W. Oosterbeek et al., *Towards absolutely calibrated ECE Michelson measurements in EC heated plasmas at W7-X*, *EPJ Web Conf.* **313** (2024) 03004.

[16] W. Kasparek et al., *Development of a polarization tuner*, Institute of Interfacial Process Engineering and Plasma Technology IGVP, Stuttgart University.

[17] M. Hirsch et al., *ECE Diagnostic for the initial Operation of Wendelstein 7-X*, *EPJ Web Conf.* **203** (2019) 03007.

[18] C. Fuchs and H.J. Hartfuß, *Technology of the new W7-AS broadband radiometer system*, *Fusion Eng. Des.* **53** (2001) 451.

[19] C. Fuchs and H.J. Hartfuß, *Extreme broadband multichannel ECE radiometer with "zoom" device*, *Rev. Sci. Instrum.* **72** (2001) 383.

[20] D. Wagner et al., *Bragg Reflection Band Stop Filter for ECE on Wega*, *J. Infrared Milli. Terahz. Waves* **32** (2011) 1424.

2025 JINST 20 C12008

[21] S.P. Hirshmann and J.C. Wilson, *Steepest-descent moment method for three-dimensional magnetohydrodynamic equilibria*, *Phys. Fluids* **26** (1983) 3552.

[22] N.B. Marushchenko, Y. Turkin and H. Maassberg, *Ray-tracing code TRAVIS for ECR heating, EC current drive and ECE diagnostic*, *Comput. Phys. Commun.* **185** (2014) 165.

[23] J.F. Guerrero Arnaiz et al., *3rd harmonic ECE for electron temperature monitoring in high-density plasmas at W7-X*, in the proceedings of the *51st EPS Conference on Plasma Physics*, Vilnius, Lithuania, Vol. 49A (2025) P4.291.

[24] J.F. Guerrero Arnaiz et al., private communication (2025).

[25] G.M. Weir et al., *Electron temperature fluctuation measurements in W7-X: Initial results from OP1.1*, in the proceedings of the *43rd EPS Conference on Plasma Physics*, Leuven, Belgium, Vol. 40A (2016) P4.009.

[26] V. Nair, *Comparison of Time Delay and Spectral Decorrelation for Detection of Electron Temperature Fluctuations in a Magnetized Plasma with Radiometry*, Dissertation KTH-Stockholm (2025) [https://urn.kb.se/resolve?urn=urn:nbn:se:kth:diva-364908].

[27] G.M. Weir et al., *Development of compact optical systems for microwave imaging in advanced experiments*, in *Basic Research Needs (BRN) Workshop on Measurement Innovation (MI)*, Washington/DC (2024) [https://www.orau.gov/brnmi2023].

[28] G.M. Weir et al., *Correlation ECE radiometry and imaging development on the stellarator Wendelstein 7-X*, in the proceedings of the *51st EPS Conference on Plasma Physics*, Vilnius, Lithuania, Vol. 49A (2025) P4.304.

[29] T. Windisch et al., *Reflectometry fluctuation diagnostics at Wendelstein 7-X*, in the proceedings of the *42nd EPS Conference on Plasma Physics*, Lisbon, Portugal, Vol. 39E (2015) P1.163.

[30] T. Windisch et al., *W-band Doppler reflectometry at Wendelstein 7-X: Diagnostic setup and initial results*, in the proceedings of the *Int. Refl. Workshop 14*, Lausanne, Switzerland (2016).

[31] T. Windisch et al., *Doppler reflectometry system upgrades for Wendelstein 7-X OP2*, in the proceedings of the *23rd International Stellarator-Heliotron Workshop*, Warsaw, Poland, 20–24 June 2022.

[32] T. Estrada et al., *Impact of magnetic islands on plasma flow and turbulence in W7-X*, *Nucl. Fusion* **61** (2021) 096011.

[33] T. Estrada et al., *Radial electric field and density fluctuations measured by Doppler reflectometry during the post-pellet enhanced confinement phase in W7-X*, *Nucl. Fusion* **61** (2021) 046008.

[34] D. Carralero et al., *Characterization of the radial electric field and edge velocity shear in Wendelstein 7-X*, *Nucl. Fusion* **60** (2020) 106019.

[35] E. Maragkoudakis et al., *On the interaction between the island divertor heat fluxes, the scrape-off layer radial electric field and the edge turbulence in Wendelstein 7-X plasmas*, *Nucl. Fusion* **63** (2023) 026011.

[36] P. Rohmann et al., *A 32-element frequency-steered array antenna for reflectometry in W-band*, in the proceedings of the *2013 IEEE International Symposium on Phased Array Systems and Technology*, Waltham, MA, U.S.A. (2013), p. 559–563 [DOI:10.1109/array.2013.6731889].

[37] T. Windisch et al., *Phased array Doppler reflectometry at Wendelstein 7-X*, *Rev. Sci. Instrum.* **89** (2018) 10H115.

[38] S. Wolf, *Development of a phased array antenna for Doppler reflectometry in fusion devices*, Ph.D. Thesis, University Stuttgart (2013).

[39] A. Krämer-Flecken et al., *Investigation of turbulence rotation in limiter plasmas at W7-X with newly installed poloidal correlation reflectometer*, *Nucl. Fusion* **57** (2017) 066023.

2025 JINST 20 C12008

[40] T. Windisch et al., *Poloidal correlation reflectometry at W7-X: radial electric field and coherent fluctuations*, *Plasma Phys. Control. Fusion* **59** (2017) 105002.

[41] S. Soldatov, A. Krämer-Flecken and C.N. Klimov, *Investigation of the poloidal spectral resolution of O-mode reflectometry with two-dimensional full-wave modeling*, *Fusion Eng. Des.* **84** (2009) 64.

[42] S. De Koker, *Characterisation of the sensitivity of poloidal correlation reflectometry single wavenumber plasma turbulence through full-wave simulation with IPF-FD3D*, M.Sc. Thesis, Unviversity Stuttgart (2025).

[43] X. Han et al., *Application of the elliptic approximation model for the edge turbulence rotation measurement via the poloidal correlation reflectometer in Wendelstein 7-X*, *Nucl. Fusion* **61** (2021) 066029.

[44] A. Krämer-Flecken et al., *Velocity modulations in view of the elliptical approach at Wendelstein 7-X*, arXiv:2503.19507 [DOI:10.1088/1361-6587/adcd2e].

[45] A. Krämer-Flecken et al., *Observation and characterisation of trapped electron modes in Wendelstein 7-X*, arXiv:2408.12900.

[46] X. Han et al., *Experimental characterization of a quasi-coherent turbulent structure in the edge plasma in Wendelstein 7-X*, *Nucl. Fusion* **60** (2020) 016011.

[47] H.M. Xiang et al., *Investigation of a low frequency coherent mode in Wendelstein 7-X with island divertor*, *Nucl. Fusion* **63** (2023) 126050.

[48] A. Krämer-Flecken et al., *Investigation of turbulence rotation in the SOL and plasma edge of W7-X for different magnetic configurations*, *Plasma Sci. Technol.* **22** (2929) 064004.

[49] J. Ongena et al., *Physics design, construction and commissioning of the ICRH system for the stellarator Wendelstein 7-X*, *Fusion Eng. Des.* **192** (2023) 113627.

[50] X. Han et al., *Development of a dual-band X-mode reflectometer for the density profile measurement at ICRH antenna in W7-X*, in the proceedings of the *14th International Reflectometry Workshop*, Lausanne, Switzerland (2019).

[51] H. Xiang et al., *Measurement and analysis of density profiles in the island divertor region and in the plasma edge of W7-X*, in the proceedings of the 49^{th} *EPS Conference on Plasma Physics*, Bordeaux, France, Vol. 47A (2023) P2.015.

[52] D. López-Rodríguez et al., *Characterization of a microwave reflectometer for edge density profile measurements at the ICRH antenna on Wendelstein 7-X*, in the proceedings of the *6th European Conference on Plasma Diagnostics*, Prague, Czech Republic (2025), to be submitted to *Plasma Phys. Control. Fusion*.

[53] J. van den Berg, I. Abramovic, N.J. Lopes Cardozo and D. Moseev, *Fast analysis of collective Thomson scattering spectra on Wendelstein 7-X*, *Rev. Sci. Instrum.* **89** (2018) 083507.

[54] D. Moseev et al., *Collective Thomson scattering diagnostic at Wendelstein 7-X*, *Rev. Sci. Instrum.* **90** (2019) 013503.

[55] D. Moseev et al., *Collective Thomson Scattering Diagnostic for Wendelstein 7-X at 175 GHz*, 2020 *JINST* **15** C05035.

[56] S. Ponomarenko et al., *Development of the 174 GHz collective Thomson scattering diagnostics at Wendelstein 7-X*, *Rev. Sci. Instrum.* **95** (2024) 013501.

[57] D. Moseev et al., *Commissioning and first results of the 174 GHz collective Thomson scattering diagnostic at Wendelstein 7-X*, 2024 *JINST* **19** C03056.

2025 JINST 20 C12008